

MICROSCALE FRACTURE PROPERTIES OF ALKALI-ACTIVATED FLY ASH

JIRÍ NĚMEČEK^{†,*}, VÍT ŠMILAUER[†], JIRÍ NĚMEČEK[†] AND JAN MAŇÁK[‡]

[†]Czech Technical University in Prague, Faculty of Civil Engineering
Prague, Czech Republic

e-mail: jiri.nemecek@fsv.cvut.cz, vit.smilauer@fsv.cvut.cz, jiri.nemecek.1@fsv.cvut.cz

[‡]Institute of Physics, Academy of Sciences
Prague, Czech Republic

e-mail: jan.manak@fzu.cz

Key words: Alkali Activated Fly Ash, Fracture, Focused Ion Beam, Microbeam, Nanoindentation, Multiscale model

Abstract. The paper shows novel methodology for the assessment of fracture properties of alkali-activated fly ash pastes. The method is based on bending of microbeams prepared by focused ion beam milling. The microbeams are fabricated in N-A-S-H gel rich regions with micrometer dimensions and loaded with the aid of nanoindenter. Young's modulus was found as 25.5 ± 4.2 GPa and tensile strength as 340.8 ± 124.1 MPa. A volumetric model for alkali-activated fly ash reconstructed three relevant phases; skeleton of fly ash, solid gel particles and open porosity. Packing density of N-A-S-H was found. A simple colloid model for strength evolution identified tensile strength of N-A-S-H solid gel particle as 2500 MPa, falling essentially on the same curve as C-S-H. N-A-S-H and C-S-H gels show similar values for Young's modulus and tensile strength, being compatible reaction products of cementitious binders.

1 INTRODUCTION

Portland clinker is as a primary binder in many concretes used in engineering structures, but industrial by-products such as fly ash, slag and various mineral admixtures are increasingly utilized as cement replacement as well. Among others, fly ash is produced in high amounts in many parts of the world as a product of coal burning in power plants. Alkali-activated systems can substitute Portland clinker to large extent [1, 2].

Nowadays, alkali-activated fly ash (AAFA) represents well-established binder with several excellent properties like chemical stability, reduced reaction heat, good elastic and strength properties similar to Portland clinker. However,

its chemical and micromechanical understanding is far away from understanding of ordinary Portland cement systems.

At lower level (nm- μ m scale), hydrated Portland cement forms a matrix composed mainly of Calcium-Silica-Hydrates (C-S-H gels), portlandite (CH), anhydrous clinker grains, capillary pores and minor constituents such as ettringite and monosulfate [3,4]. Due to the local nucleation of hydrates from clinkers variable stoichiometry and density develops in the hydrated paste. Two characteristic packing densities of the main hydration product (C-S-H gel) have been differentiated in the past, high (HD C-S-H) and low (LD C-S-H) [5]. The average packing density of the HD structure is 0.74 while it is less than 0.64 for the LD structure [5–7]. Such

findings were demonstrated also by nanoindentation [8].

In contrast, AAFA pastes are created by a sol-gel process involving poly-condensation of a solution as the main underlying chemical reaction [1]. The reaction product is sodium aluminosilicate gel (N-A-S-H gel) which poses no characteristic porosity [9]. The reaction of AAFA in ambient conditions is much slower compared to cement hydration under room temperature. After 28 days, the degree of hydration of usual cement paste with water to cement ratios of 0.4-0.6 is about 0.6-0.8 while for AAFA is only about 0.2 [9]. Therefore, the reaction of AAFA is often accelerated by thermal treatment.

Mechanical characterization of individual phase constituents of cement paste or AAFA at micrometer scale have been performed by means of nanoindentation [10]. Many engineering properties such as elastic moduli, hardness, short-term creep can be derived from standard nanoindentation measurements that are performed in prevailing compression stress states. In contrast, tension properties or fracture energy cannot be directly measured by nanoindenters.

A new technique combining nanoindentation with fabrication of micromachined beams have been developed a few years ago. The technique employs focused ion beam milling (FIB) for fabrication of cantilever microbeams that can be subsequently bent by a nanoindenter. The technique have been tested previously on Portland cement pastes [11]. Here, we adopt the methodology for AAFA samples.

2 EXPERIMENTAL PART

2.1 Samples and preparation

As a raw material, fly ash (class F) originating from brown coal power plant Opatovice (Czech Republic) was used. It has specific Blaine surface $210 \text{ m}^2/\text{kg}$. The XRD Rietveld analysis yielded the composition of 70 vol.% amorphous phases, 24 vol.% mullite, and 6 vol.% quartz. The chemical composition is shown in Table 1.

Table 1: The chemical composition of fly ash

SiO ₂	Al ₂ O ₃	Fe ₂ O ₃	CaO	TiO ₂	K ₂ O
51.9	32.8	6.3	2.7	1.89	2.12

The fly ash was mixed with an alkali-activator which was prepared by dissolving NaOH pellets in tap water and by adding sodium silicate (water glass). Resulting mixture was characterized by mass oxide ratio of an activator and activator-to-solid mass ratio as: $\text{Na}_2\text{O}/\text{SiO}_2=0.881$, $\text{H}_2\text{O}/\text{Na}_2\text{O}=3.068$, $\text{activator}/\text{solid}=0.456$. After mixing, samples were cured at 80°C for 12 h and then stored in laboratory conditions (22°C) until testing. Prior to further analyses, the samples were cut into 5 mm thick slices and prepared with a metallographic procedure [10, 11] to get a flat and smooth surface with small roughness of several tens of nm. Samples were tested at the age of 7 months.

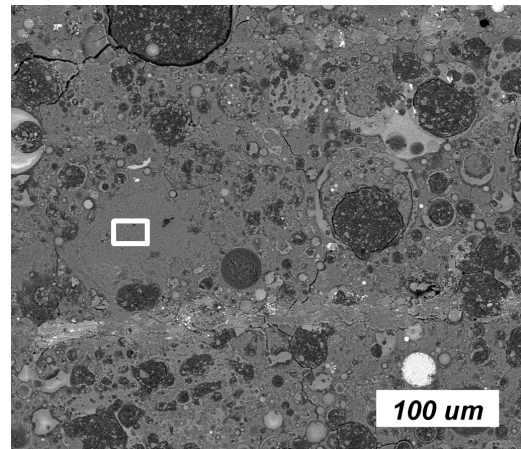


Figure 1: AAFA microstructure (white box indicates location of a future microbeam).

2.2 FIB and loading of microbeams

First, the samples were scanned in scanning electron microscope (SEM) and locations of individual microstructural phases detected. An example of sample microstructure is shown in Figure 1. From the morphological observations, locations with N-A-S-H gel were identified and a dozen of small micro-beams was prepared with FIB technology. FEI Quanta 3D FEG dual

beam instrument combining SEM and FIB was used for fabrication of all the samples. The FIB technique uses finely focused beam of gallium ions for precise milling of microscopic samples with various geometries. Based on previous studies [11], the sample geometry was chosen to be a cantilever beam of 20 μm length and triangular cross-section with approximate dimensions of 3-4 μm in height and width. The final milling step was done at an accelerating voltage of 30 kV and a current of 0.1 nA. After FIB milling, the micro-beams were observed by SEM to scan their actual dimensions and positions. An example of a milled beam is shown in Figure 2.

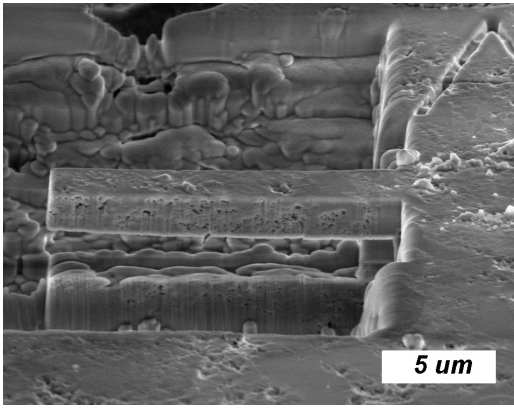


Figure 2: Microbeam milled by FIB in N-A-S-H gel.

2.3 Nanoindentation and mechanical properties

Nanoindenter (Hysitron TI-700) equipped with Berkovich tip and in-situ scanning capability was used to position the tip on the free end of the cantilever microbeam. Then, the microbeam was bent in a few elastic cycles and then deformed until fracture. The bending was performed in the displacement control regime. The nanoindenter provided records of deflection and load over the whole test. Using beam theory, Young's modulus of the beam can be assessed as

$$E = \frac{FL^3}{3wI_y} \quad (1)$$

where F and w are the force and deflection reached in the elastic regime, respectively, L is

the micro-beam length, I_y the second moment of inertia of the cross section. Tensile strength was calculated from the ultimate cycle as

$$f_t = \frac{F_{max}L}{W_h} \quad (2)$$

where F_{max} is the maximum measured force, W_h is the section modulus. Fracture energy was calculated according to the methodology used in [11] as

$$G_f^{sup} = \frac{1}{A_f} \int_0^{w_{max}} Fdw \quad (3)$$

where w_{max} is the peak deflection and A_f is the nominal fracture area (measured by SEM after the break). It should be noted that the stability of the measurement in the displacement controlled regime depends on the system stiffness and on the sampling frequency of the feedback control. For fast events of a brittle failure it puts high requirements to the system that is not capable to capture descending (softening) branch in majority of the cases. The system is also not capable to capture snap-back behavior. Thus, the fracture energy was, in accordance with [11] assessed as supremum energy assuming that micro-beam behavior shows neither snap-back nor softening.

2.4 Experimental results and discussion

Load-deflection curves were obtained on a dozen of microbeams prepared in N-A-S-H gel. Behavior of the beams was close to linear up to the break with sudden descending branch (in case of control instability) or a slightly softening branch (in case of stable softening measurement). Examples of loading diagrams that are normalized with respect to the beam length are depicted in Figure 3. Mechanical parameters obtained from the testing of microbeams are summarized in Table 2; for comparison, outer C-S-H gel is reported as well [11].

Elastic moduli of microbeams calculated from Equation (1), 25.5 ± 4.2 GPa, are in good agreement with literature data of N-A-S-H based, e.g. from nanoindentation [10]. Also, the value corresponds well with outer product of cement pastes ($E_{cem-op} = 24.9 \pm 1.3$ MPa, [11]).

Tensile strengths of N-A-S-H, 340.8 ± 124.1 MPa, are much higher than macroscale strength, which attains up to 10 MPa on millimeter sized samples. The discrepancy between the scales can be explained by a multiscale model that takes into account other phases and defects (see Section 3). N-A-S-H gel strength and supremum fracture energy are also comparable to outer product of Portland cement paste ($f_{t,cem-op}=264.1 \pm 73.4$ MPa, $G_f^{sup}=4.4 \pm 1.9$, [11]).

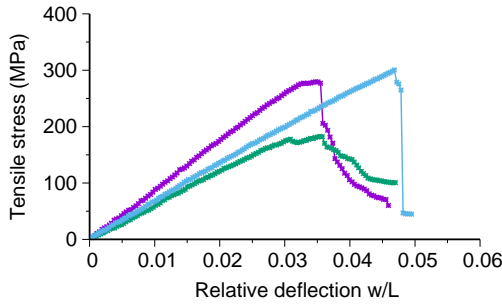


Figure 3: Examples of loading diagrams of microbeams in N-A-S-H gel.

Table 2: Results from microbeams' bending. N-A-S-H gel and outer C-S-H gel

	E (GPa)	f_t (MPa)	G_f^{sup} (J/m ²)
N-A-S-H gel	25.5 ± 4.2	340.8 ± 124.1	4.5 ± 1.8
Outer C-S-H gel	24.9 ± 1.3	264.1 ± 73.4	4.4 ± 1.9

3 MICROMECHANICAL MODEL

Micromechanical model for strength scaling stems from volumetric fraction of three relevant phases [9]:

Skeleton of fly ash denoted as f_{FA}^{Skel} . Corresponds to unreacted fly ash.

Solid gel particles denoted as f_{SGP} . N-A-S-H gel is treated as a agglomeration of solid gel particles in the sense of a colloid model.

Open porosity is initially filled with an activator and also by pores closed inside unreacted fly ash. Open porosity decreases slowly over time with advancing degree of reaction.

Thermal curing 12 h at 80°C speeds up reaction time 225× with regards to 25°C curing temperature (based on Arrhenius energy of 86.2 kJ/mol [9]), reaching equivalent time 112.5 days and degree of reaction $DoR = 0.46$. Before the testing at 7 months, the samples were stored sealed at 20°C, reaching equivalent time of 229 days and $DoR = 0.574$. Those equivalent times lead to volumetric model of the phases [9] as:

$$f_{FA}^{Skel} = 0.581 \cdot (1 - 0.574) = 0.248 \quad (4)$$

$$f_{SGP} = (0.581 + 0.224) \cdot 0.574 = 0.462 \quad (5)$$

$$f_{OP} = 0.290 \quad (6)$$

$$f_{FA}^{Voids} = 0 \quad (7)$$

which are showed graphically in Figure 4.

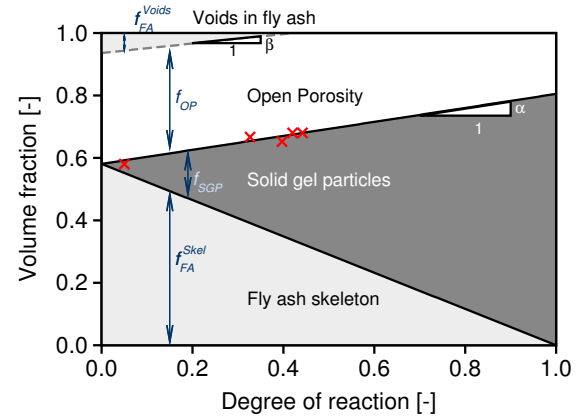


Figure 4: Volumetric model of alkali-activated fly ash [9].

Open porosity contains all pore ranges; from air-entrapped pores up to sub-nm pores accessible by n -octane. Total value of open porosity corresponds well with He-pycnometry and gives slightly higher values than results from MIP porosimetry [9]. Since N-A-S-H gel has no characteristic porosity (it is not a precipitate like C-S-H), the average packing density of N-A-S-H gel is evaluated as $f_{SGP}/(f_{SGP} + f_{OP}) = 0.462/(0.462 + 0.290) = 0.614$.

3.1 Material model for compressive and tensile failure

Material model describing compressive or tensile failure at each level is based on fracture/damage mechanics. Damage mechanics uses the concept of an equivalent strain, $\tilde{\varepsilon}$, as a descriptor of damage evolution. Damage becomes initiated when the equivalent strain, $\tilde{\varepsilon}$, exceeds strain at the onset of cracking, $\varepsilon_0 = f_t/E$, where E is the elastic modulus. The Rankine criterion for tensile failure defines $\tilde{\varepsilon}$ as

$$\tilde{\varepsilon} = \frac{\sigma_1}{E}, \sigma_1 > 0 \quad (8)$$

where σ_1 is the maximum positive effective principal stress of undamaged-like material. Figure 5 elucidates the mechanism.

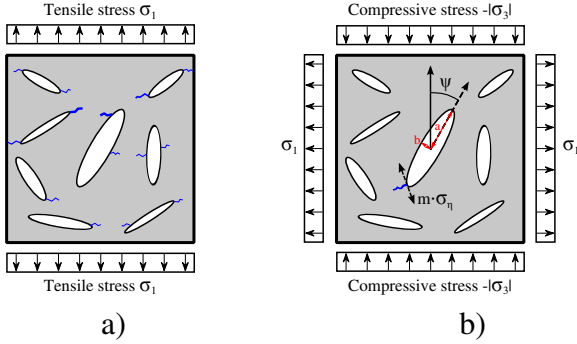


Figure 5: Crack evolution during (a) uniaxial tensile stress and (b) compressive stresses. The material contains randomly oriented elliptical voids with negligible area.

Under uniaxial compressive stress, crack initiation occurs under a different mechanism. A homogeneous material experiences only one negative principal stress and deviatoric stresses. Cracking in diagonal, shear band zone, is often encountered on cementitious specimens, however, the physical mechanism is again tensile microcracking in voids and defects in the underlying microstructure [12, pp.297]. Such a behavior has already been described in the work of Griffith [13], and McClintock and Walsh [14], and we briefly review this theory and extend it with an equivalent strain to be used in the framework of damage mechanics.

It is assumed that a material contains randomly oriented 2D elliptical flat voids with various aspect ratios $m = b/a$. The voids have

a negligible area and only represent stress concentrators and internal defects in a material. Under macroscopic biaxial stress, the maximum tensile stress among all voids, $m \cdot \sigma_\eta$, appears on a critically inclined elliptical void under a critical angle ψ

$$\cos 2\psi = \frac{\sigma_3 - \sigma_1}{2(\sigma_3 + \sigma_1)}, \frac{\sigma_1}{\sigma_3} \geq -\frac{1}{3} \quad (9)$$

$$m \cdot \sigma_\eta = \frac{-(\sigma_1 - \sigma_3)^2}{4(\sigma_1 + \sigma_3)} \quad (10)$$

Crack formation occurs when the tangential tensile stress, $m \cdot \sigma_\eta$, equals to the tensile strength of the matrix. Since σ_η and the crack geometry, m , cannot be measured directly, it is reasonable to relate their product to the uniaxial macroscopic tensile stress, $\bar{\sigma}_1$, as proposed by Griffith [13]

$$\bar{\sigma}_1 = \frac{m \cdot \sigma_\eta}{2} \quad (11)$$

The material starts to crack when $\bar{\sigma}_1$ equals to the uniaxial macroscopic tensile strength f_t . Note that the tensile strength of the homogeneous matrix (intrinsic strength) and the crack geometry remain unknown separately and we can assess only apparent macroscopic tensile strength f_t .

Plugging Equation (10) into Equation (11) and further into Equation (8) leads to the definition of the equivalent strain, $\tilde{\varepsilon}$, under compression-dominant loading

$$\tilde{\varepsilon} = \frac{1}{E} \cdot \frac{-(\sigma_1 - \sigma_3)^2}{8(\sigma_1 + \sigma_3)} \quad (12)$$

An interesting feature of the Griffith model is that the ratio of the uniaxial compressive-to-tensile strength equals to 8

$$|f_c| = 8f_t \quad (13)$$

This can be verified when plugging $\sigma_1 = f_t$ into Equation (8) which leads to $\tilde{\varepsilon} = f_t/E$. Plugging $\sigma_1 = 0$, $\sigma_3 = -8f_t$ into Equation (12) leads to the same equivalent strain.

Since the equivalent strain may arise from the Rankine or Griffith criterion, it is necessary to compare both Equations (8) and (12) and to

select the higher equivalent strain. Linear softening is assumed in the simulations and damage evolution law has a small effect on the computed macroscopic strength. The linear cohesive law takes the form

$$\sigma = f_t \left(1 - \frac{w}{w_f}\right) \quad (14)$$

where w is a crack opening and w_f is the maximum crack opening at zero stress. According to the formulation of the isotropic damage model, the uniaxial tensile stress obeys the law

$$\sigma = (1 - \omega)E\tilde{\varepsilon} \quad (15)$$

Let us consider the fracture energy in mode I, G_f , and the effective thickness of a crack band h , which corresponds to the finite element size in the direction of the maximum principal strain [12]. This ensures objective results, independent on finite element size [15]. Notice that $w = h\omega\tilde{\varepsilon}$ and $w_f = 2G_f/f_t$. The evolution of isotropic damage is obtained by combining Equations (14) and (15)

$$\omega = \left(1 - \frac{\varepsilon_0}{\tilde{\varepsilon}}\right) \left(1 - \frac{hE\varepsilon_0^2}{2G_f}\right)^{-1} \quad (16)$$

3.2 Model for fracture properties of N-A-S-H gel

N-A-S-H gel is treated as a colloid, composed of solid gel particles with varying porosity. Packing density describes conveniently volume fraction of solid gel particles in a unit cell. Our model used 3D and 2D images for different packing densities, η ; Figure 6 shows two 3D examples used for $\eta = 0.63$ and $\eta = 0.76$, corresponding to C-S-H_{LD} and C-S-H_{HD} [7].

Unit cell representing $100 \times 100 \times 200$ nm uses periodic boundary conditions on horizontal surfaces and uniform static boundary conditions with zero normal stress on vertical surfaces. Vertical eigenstrain loads the unit cell and uniaxial macroscopic tensile stress is obtained by spatial averaging.

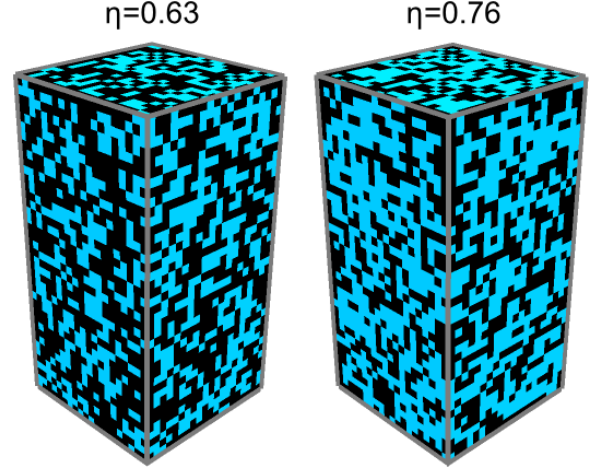


Figure 6: Unit cells for two packing densities, $20 \times 20 \times 40$ brick elements, representing $100 \times 100 \times 200$ nm.

Figure 7 displays the evolution of the N-A-S-H gel strength with regards to its packing density. Fracture energy 2 J/m^2 was assigned to the globule and the simulation used simplified 2D microstructure of 200×200 nm. Analytical approximation reads

$$f_{t,NASH} = 2500 \exp\left(\frac{1.293(\eta^{13.011} - 1)}{\eta}\right) \quad (17)$$

where intrinsic tensile strength of a solid gel particle was found as 2500 MPa. The same value was used previously for assessing C-S-H_{LD} and C-S-H_{HD} tensile strength, falling essentially on the same curve [16].

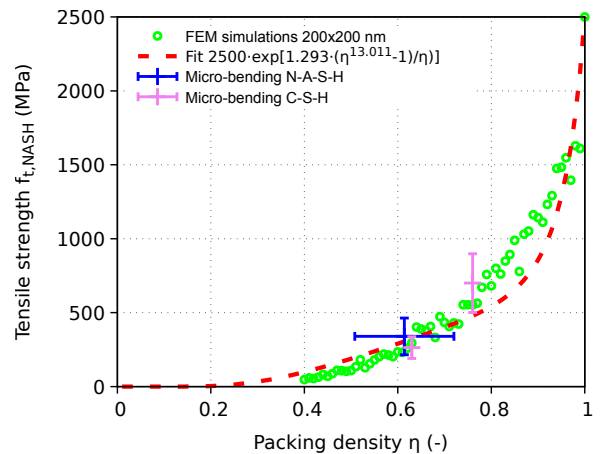


Figure 7: Scaling of tensile strength in N-A-S-H gel.

Tensile strength of N-A-S-H gel shows high standard deviation, 340.8 ± 124.1 MPa. This

demonstrates high heterogeneity on the scale on several μm , comparable with the size of the bent beams. Such standard deviation leads to different packing densities, in our particular case to 0.614 ± 0.106 when comparing to micromechanically-simulated data in Figure 7.

The size of fracture process zone of N-A-S-H gel can be obtained from different underlying assumptions. Non-linear fracture process zone's size ahead of the crack tip falls in the range from Irwin's $1/\pi$ to 5 for concrete [12, pp. 107] which yields

$$R_c = k \frac{EG_f}{f_t^2} = \left(\frac{1}{\pi} \div 5 \right) \frac{25.5 \cdot 4.5}{340.8^2} \cdot 1000 = 0.31 \div 4.9 \mu\text{m} \quad (18)$$

3.3 Model for fracture properties of AAFA paste

AAFA paste spans the range from approximately $1 \mu\text{m}$ to $100 \mu\text{m}$. Since all the open porosity has been already assigned to underlying N-A-S-H level, paste level can reduce tensile or compressive strength by

- strength variation of N-A-S-H gels, or
- crack formation in the binder

Spatial strength variation of N-A-S-H gel points to weaker regions with lower packing density of solid gel particles. This mimic situation of outer C-S-H mixed with capillary porosity. Weaker spots in the microstructure leads to strain localization and crack initiation. Up to date, spatial variation with corresponding fluctuation length has not been quantified and waits for further experimental tests.

It has been showed previously that a single crack of 1.5 mm length reduces tensile strength of cement paste to approximately 20% [17]. Experimental data are missing on this topic as well, especially on sub-mm samples where bending strength can be easily accessed.

4 CONCLUSIONS

The paper shows novel methodology based on nanoindentation and FIB for the assessment of small scale fracture properties of alkali-activated fly ash pastes. It provides tensile strength and fracture energy of N-A-S-H gel at the level of micrometers. It was found that tensile strength on this scale is $340.8 \pm 124.1 \text{ MPa}$ and the specific fracture energy lies in the range of units of J/m^2 . N-A-S-H gel mechanical response was found to be similar to outer product in cement paste in terms of elasticity and tensile strength, showing nice compatibility with C-S-H.

Micromechanical models showed that N-A-S-H gel can be treated as a colloid with packing density of solid gel particles. Tensile strength falls essentially on the same curve as for C-S-H gels, supporting the idea that N-A-S-H gels have the same strength origin of C-S-H.

5 ACKNOWLEDGEMENT

Financial support of the Czech Science Foundation (project 17-05360S) and the Czech Technical University in Prague (SGS18/114/OHK1/2T/11, SGS19/032/OHK1/1T/11) is gratefully acknowledged.

REFERENCES

- [1] Provis, J. L. and van Deventer J. S. J. (Eds.) 2009. *Geopolymers: Structures, Processing, Properties and Industrial Applications*. Woodhead Publishing Ltd, first edition.
- [2] Shi, C., Krivenko, P. V., and Roy, D. 2006. *Alkali-activated cements and concretes*. Taylor & Francis, first edition.
- [3] Taylor, H. F. W. 2003. *Cement Chemistry, Second Edition*, Thomas Telford.
- [4] Mehta, P. K. and Monteiro, P. J. M. 2014. *Concrete: Microstructure, Properties, and Materials*, McGraw-Hill (4th ed.)

- [5] Jennings, H.M. 2000. A model for the microstructure of calcium silicate hydrate in cement paste. *Cement and Concrete Research* **30(1)**:101 - 116.
- [6] Jennings, H.M. 2008. Refinements to colloid model of C-S-H in cement: CM-II. *Cement and Concrete Research* **38(3)**:275 - 289.
- [7] Constantinides, G. and Ulm, F.-J. 2007. The nanogranular nature of C–S–H. *Journal of the Mechanics and Physics of Solids* **55(1)**:64 - 90.
- [8] Constantinides, G. and Ulm, F.-J. 2007. The effect of two types of C-S-H on the elasticity of cement-based materials: Results from nanoindentation and micromechanical modeling. *Cement and Concrete Research* **34(1)**:67 - 80.
- [9] Šmilauer, V., Hlaváček, P., Škvára F., Šulc R., Kopecký, L., and Němeček, J. 2012. Micromechanical multiscale model for alkali activation of fly ash and metakaolin. *Journal of Materials Science*, **46(20)**:6545–6555.
- [10] Němeček, J., Šmilauer, V., Kopecký, L. 2011. Nanoindentation characteristics of alkali-activated aluminosilicate materials. *Cement and Concrete Composites* **33(2)**:163 - 170.
- [11] Němeček, J., Králík, V., Šmilauer, V., Polívka, L., Jäger, A. 2016. Tensile strength of hydrated cement paste phases assessed by micro-bending tests and nanoindentation. *Cement and Concrete Composites* **73**:164 - 173.
- [12] Bažant, Z. P. and Planas, J. 1998. *Fracture and Size Effect in Concrete and Other Quasibrittle Materials*. CRC Press.
- [13] Griffith, A. 1924. Theory of rupture. In Biezeno, C. and Burgers, J., editors, *First International Congress for Applied Mechanics*, 55 – 63, Delft.
- [14] McClintock, F. and Walsh, J. 1962. Friction of griffith cracks in rock under pressure. In *Proc. Fourth U.S. National Congress of Applied Mechanics*, 1015 – 1021, New York City.
- [15] Jirásek, M. and Bažant, Z. P. 2002. *Inelastic analysis of structures*. John Wiley & Sons, Ltd.
- [16] Němeček, J., Šmilauer, V., Němeček, J., Kolařík, F., and Maňák, J. 2018. Euro-c 2018. In Meschke G, Pichler B, R. J., editor, *Computational Modelling of Concrete Structures*, Bad Hofgastein, Austria. Boca Raton, USA.
- [17] Šmilauer, V., Kolařík, F., Němeček, J., and Maňák, J. 2018. Strength scaling from C-S-H globules to cement paste using multiscale hierarchical modeling. In *Proceedings of the Workshop on Concrete Modelling and Materials Behaviour in honor of Professor Klaas van Breugel*. Rilem Publications S.A.R.L.